wire were much larger, on a per-carbon basis, than that of the surrounding alkanethiols. However, experiments (*10*) on single molecules with attached NPs show that this is not the case.

23. X. D. Cui *et al.*, *Nanotechnology* **13**, 5 (2002).
24. D. J. Wold, C. D. Frisbie, *J. Am. Chem. Soc.* **123**, 5549 (2001).
25. See the supporting information on *Science* Online.
26. L. H. Dubois, R. G. Nuzzo, *Annu. Rev. Phys. Chem.* **43**, 437 (1992).
27. A. Ulman, *Chem. Rev.* **96**, 1533 (1996).
28. Supported by a Nanoscale Interdisciplinary Research Teams award of NSF. We thank D. Gust, A. Moore, T. Moore, O. F. Sankey, J. Tomfohr, X. Zarate, G. Kada, R. Tsui, and H. Goronkin for helpful discussions and J. Robinson for assistance with data analysis.

Supporting Online Material
www.sciencemag.org/cgi/content/full/300/5624/1413/DC1
Figs. S1 to S5

24 February 2003; accepted 23 April 2003

Real-Time Monitoring of Growing Nanoparticles

Gilles Renaud,[1]* Rémi Lazzari,[1,2] Christine Revenant,[1] Antoine Barbier,[1] Marion Noblet,[1] Olivier Ulrich,[1] Frédéric Leroy,[1] Jacques Jupille,[2] Yves Borensztein,[3] Claude R. Henry,[4] Jean-Paul Deville,[5] Fabrice Scheurer,[5] Jeannot Mane-Mane,[5] Olivier Fruchart[6]

One challenge in the production of nanometer-sized objects with given properties is to control their growth at a macroscopic scale in situ and in real time. A dedicated ultrahigh-vacuum grazing-incidence small-angle x-ray scattering setup has been developed, yielding high sensitivity and dynamics. Its capabilities to derive the average particle shape and size and the film growth mode and ordering and to probe both surfaces and buried interfaces are illustrated for two prototypical cases: the model catalyst Pd/MgO(100) and the self-organized Co/Au(111) system. A wide range of technologically important systems can potentially be investigated in various gaseous environments.

Nanometer-sized islands that are grown on substrates display new properties that are of interest for both basic and applied research. These islands include model catalysts made of supported metallic particles whose reactivity and selectivity can be adapted to given needs (*1–3*), single-domain magnetic particles that show original spin-dependent transport properties (*4*), and coherently strained semiconductor aggregates, the so-called "quantum dots," that exhibit remarkable optoelectronic properties [for a review, see (*5*)]. The potential for new device applications is dependent on the ability to control the shape, size, and ordering of the nanoparticles. This points to the importance of controlling the growth of large collections of nanoparticles by monitoring the relevant parameters in situ and in real time (*3*). Near-field scanning microscopy suffers from the need for long acquisition times and the interruption of the growth process. A statistical investigation in reciprocal space by grazing-incidence small-angle x-ray scattering (GISAXS) (*6–8*) appears directly relevant for coping with this issue, but technical limitations have prevented the in situ use of this method during particle growth. In this report, the capability of a dedicated device to analyze growing particles and particle-substrate interactions is illustrated in two cases: Pd on MgO(001), a model system of Volmer-Weber [three- dimensional (3D)] growth of metal on oxide surfaces, which is important in the investigation of the elementary processes of heterogeneous catalysis (*2*); and the self-organized growth of Co nanodots on the herringbone reconstructed Au(111) surface (*9*).

The principles behind GISAXS are shown in Fig. 1. A narrow and well-collimated incident x-ray beam is directed toward the surface at a grazing angle α_i, close to the critical angle for total external reflection, and is scattered by nanometer-sized heterogeneities of the electron density, such as islands. To first order (*10*), the GISAXS intensity is proportional to the form factor $F(\mathbf{q})$ times the interference function $S(\mathbf{q})$, where $\mathbf{q}$ is the momentum transfer. $F(\mathbf{q})$ and $S(\mathbf{q})$ are the Fourier transforms of the particle shape and the island-island pair correlation function (i.e., the probability that two islands are separated by a given vector), respectively. The average particle lateral size d and height h are thus inversely proportional to the spread of the scattering, parallel and perpendicular to the surface, respectively. The average island separation D is inversely proportional to the distance between the main spots along the parallel direction (*6*).

This setup (*11*) was developed at the European Synchrotron Radiation Facility (ESRF). We achieved nearly background-free measurements by the direct coupling of an ultrahigh-vacuum chamber with the synchrotron ring, thus avoiding scattering elements along the pathway of the x-ray beam (figs. S1 to S3). The scattered intensity was measured on a 2D charge-coupled device detector placed perpendicular to the incident beam. Double focusing of the monochromatic beam yielded very large intensity dynamics (about a few tens of thousands). GISAXS measurements for equivalent thickness Θ (the thickness of a hypothetical 2D layer of the same amount of deposited material) as low as 0.01 nm could be performed within a few seconds. At higher coverage, patterns could be recorded in a few tenths or hundredths of a second, so that the growth could be shown as a movie in real time (*11*) (movie S1).

The determination of growth laws requires simultaneous knowledge of the particle profile and of the average values of the particle size and distances, which means direct observations during growth. During the growth (Fig. 2A) of Pd films (from 0.1 nm to 2.8 nm thick) deposited at 650 K on MgO(001) (*11*), the shrinkage of the scattered intensity toward the origin of the reciprocal space with increasing film thickness revealed continuous island growth in all real-space directions (Fig. 2B). This is expected for a pro-

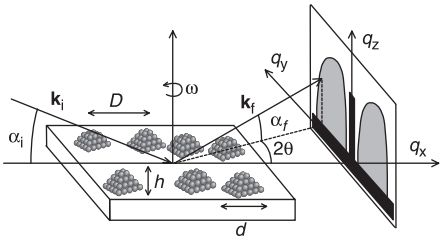

Fig. 1. The principles behind GISAXS. $\mathbf{k}_i$ and $\mathbf{k}_f$ are the incident and scattered wave vectors, respectively, yielding the momentum transfer (i.e., the reciprocal space vector) $\mathbf{q} = \mathbf{k}_f - \mathbf{k}_i$. The angles α_i, α_f, and 2θ are related to the components of the momentum transfer, either parallel (q_x and q_y) or perpendicular (q_z) to the sample surface, by the equations $q_x = |\mathbf{k}_i|[\cos 2\theta \cos\alpha_f - \cos\alpha_i]$, $q_y = |\mathbf{k}_i|[\sin 2\theta \cos\alpha_f]$, and $q_z = |\mathbf{k}_i|[\sin\alpha_f + \sin\alpha_i]$. Close to the origin in reciprocal space because they are small, the in-plane and out-of-plane scattering angles, 2θ and α_f scale with the components q_y and q_z of $\mathbf{q}$. The sample can be rotated around its surface normal by an ω rotation, which defines the orientation of the incident x-ray beam with respect to the in-plane crystallographic directions. A beam stop protects the bidimensional detector from the direct and reflected beams.

[1]Département de Recherche Fondamentale sur la Matière Condensée/Service de Physique des Matériaux et des Microstructures, Commissariat à l'Energie Atomique Grenoble, 38054 Grenoble Cedex 09, France. [2]Groupe de Physique du Solide, Universités Paris 6 et Paris 7, 2 place Jussieu, 75251 Paris Cedex 05, France. [3]Laboratoire d'Optique du Solide, CNRS, and Université Paris 6, case 80, 4 place Jussieu, 75252 Paris Cedex 05, France. [4]Centre de Recherche sur les Mécanismes de la Croissance Cristalline-CNRS, Campus de Luminy, case 913, 13288 Marseille Cedex 09, France. [5]Institut de Physique et Chimie des Matériaux de Strasbourg, Unité Mixte de Recherche 7504 CNRS–Université Louis Pasteur, 23 rue du Loess, 67037 Strasbourg Cedex, France. [6]Laboratoire Louis Néel, boîte postale 166, 38042 Grenoble Cedex 9, France.

*To whom correspondence should be addressed. E-mail: grenaud@cea.fr

cess of nucleation, growth, and finally coalescence of islands.

The emergence (at $\Theta \sim 0.2$ nm) of a rod of scattering at 54.7° with respect to the surface normal (i.e., along the {111} directions) when the incident beam was along the <110> directions, together with the absence of a rod when the beam was along the <100> directions (Fig. 3A), shows the existence of {111} facets on the Pd islands. The emergence of second- ($\Theta \sim 0.4$ nm) and third- ($\Theta \sim 1$ nm) order scattering peaks perpendicular to the surface indicated flat Pd(001) terraces. These features pointed to a truncated, octahedron-like, average particle shape with {100} and {111} facets. This is consistent with previous observations (*2*, *12*) of the growth of Pd on MgO(001), as well as with transmission electron micrographs (Fig. 2C) of the final deposit (although this 2.8-nm-thick deposit displayed additional rectangular-like particles resulting from the coalescence of smaller islands). It is also consistent with quantitative analysis (Fig. 3) performed with a dedicated program code, (*13*) based on the distorted-wave Born approximation (*10*), of the GISAXS patterns (Fig. 3A) obtained on the 1.5-nm-thick Pd grown at 650 K (before coalescence) to ensure that islands shared a common shape (*2*, *12*). Four cuts were simultaneously used to fit the data (Fig. 3B). Many different average particle shapes were tried, such as truncated pyramids and faceted spheres. The best fit was obtained with a truncated octahedron (Fig. 3C), that yielded $d = 12.6 \pm 0.4$ nm with a log-normal distribution of 6 nm full width at half maximum (FWHM), $D = 21 \pm 0.2$ nm (*14*), $h_{(001)} = 5.8 \pm 0.1$ nm, and a total height of $h = 7.9 \pm 0.1$ nm with a distribution of 0.8 ± 0.4 nm FWHM (*15*). The average thickness recalculated from these parameters was exactly the calibrated thickness of 1.5 nm (*16*). The function $S(\mathbf{q})$ presented a broad peak and rapidly tended to 1 as q_y increased, indicating a disordered arrangement of the particles. The 2D image (Fig. 3D) simulated with these parameters compares very well with the experimental image. The second and third maxima perpendicular to the surface are well reproduced, as well as the four orders of magnitude of intensity variation (*17*). The specular intensity (along the q_z axis, for very small q_y) was not simulated, because it contains information on the average film thickness but not on the islands.

An important point is that the ratio $h_{(001)}/d$ was found to be constant (0.46) and equal to the calculated value $[0.5 \times \sin(\theta) \times \sigma_{(001)}/\sigma_{(111)}]$ according to the Wulff-Kaishew's construction (*18*, *19*), in which $\sigma_{(001)} = 1.64$ J/m^2 and $\sigma_{(111)} = \sqrt{3}/2 \times \sigma_{(001)}$ (*20*) are the specific surface energies of the (001) and (111) facets and θ (54.7°) is the angle between them. The total aspect ratio $h/d \sim 0.62 \pm 0.02$ (Fig. 2B) was also found to be constant throughout the deposition time, up to $\Theta \sim 1.5$ nm. These two observations show that, up to $\Theta \sim 1.5$ nm, the particles are close to equilibrium shape. This allows the determination, by means of Wulff-Kaishew's theorem, of the adhesion energy β, which could otherwise be derived only from ex situ measurements

$$\beta = 2\sigma_{(100)}\left[1 - h/d \times \frac{\sigma_{(111)}}{\sigma_{(100)}} \times \sin^{-1}(\theta)\right]$$

This yields $\beta = 1.12$ J/m^2, which compares

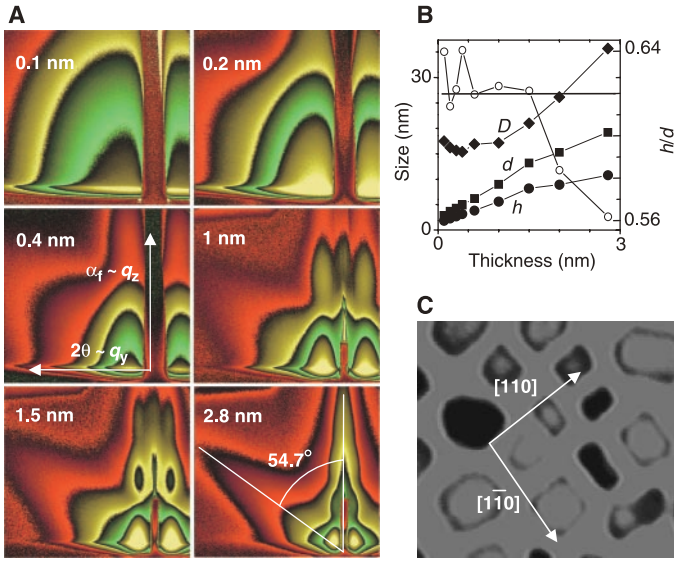

Fig. 2. In situ GISAXS measurements during Pd deposition on MgO(001) at 650 K. (**A**) GISAXS patterns for different thicknesses, with the incident beam along the MgO[110] direction. The vertical direction is perpendicular to the sample surface, and the horizontal direction is parallel. The intensity scale is logarithmic. Colors separated by black shades correspond to orders of magnitude. The exposure time was chosen to limit the peak intensity to a few tens of thousands of counts per pixel, the average background being below one count per pixel. The first images were recorded in a few seconds with a large beam stop, whereas the last were recorded with a narrower beam stop in some tens of milliseconds. (**B**) Left scale: The evolution of island spacing D (solid diamonds), lateral size d (solid squares), and height h (solid circles) with equivalent thickness Θ, as deduced from analysis of the GISAXS data, with a truncated octahedron as the average island shape. Right scale: Evolution of the aspect ratio h/d (open circles). (**C**) Ex situ TEM image (250 nm by 250 nm) of the last, 2.8-nm-thick deposit, after carbon coating and substrate dissolution. At 2.8 nm, the polydispersity is large, in particular because of the coalescence of neighboring islands. It is expected to be smaller (*2*) for the 1.5-nm equivalent thickness deposit analyzed, which corresponds to the end of the growth stage, just before coalescence starts.

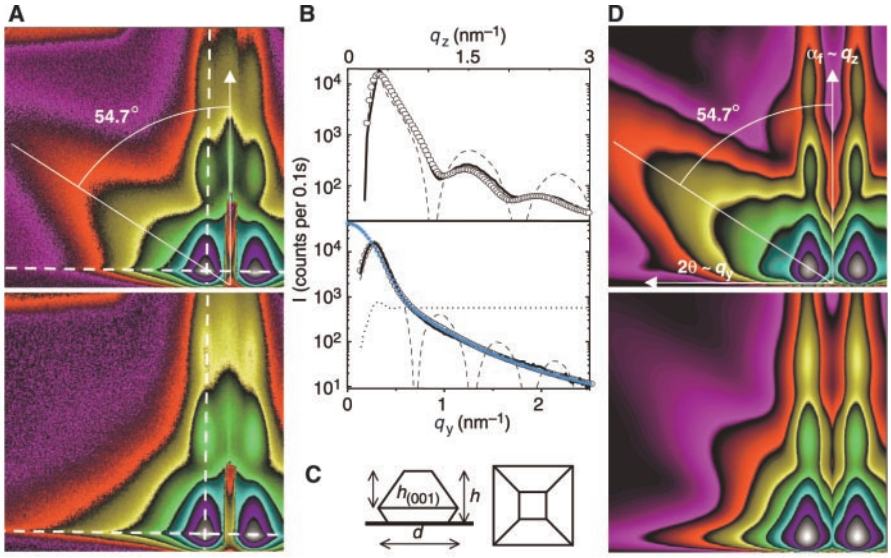

Fig. 3. A 1.5-nm-thick Pd deposit on MgO(001) at 650 K. (**A**) GISAXS images recorded in 0.1 s with the incident beam along the MgO[110] (top) and [100] (bottom) directions. White dotted lines show the positions of the four cuts simultaneously used to fit the data, perpendicular and parallel to the surface. (**B**) Best fit of the cuts (continuous lines) perpendicular (top) and parallel (bottom) to the surface in (A, bottom), with (circles) and without (dashed lines) size distribution, for a truncated octahedron. In the parallel cut (bottom), the averages of the square of the structure factor appear as blue diamonds. The fitted interference function $S(\mathbf{q})$ (dotted line) is reported on an arbitrary scale. I, intensity. (**C**) Schematic drawing of the fitted, truncated octahedron shape. (**D**) Simulated GISAXS images obtained after simultaneous fitting of the four experimental cuts. The specular reflectivity (close to $q_y = 0$) was not calculated.

well with the experimental values derived from both sessile drop measurements (0.947 J/m^2) (*21*) and electron microscopy analysis (0.91 J/m^2) (*12*).

The nucleation density (inversely proportional to D^2) can be derived from the mean inter-island distance D (Fig. 2B). D first decreased for Θ ranging from 0.0 to 0.4 nm (the nucleation stage), then stayed constant between 0.4 and 1.5 nm (the continuous growth stage), and finally increased (the coalescence stage) (*22*). During the growth stage, particles had a small polydispersity and a constant density, whose small value (6×10^{11} cm^{-2}) demonstrates a random nucleation without pinning on point defects (*12*, *22*). In the last two stages, we found a power-law growth of the mean diameter with time t (which here was proportional to Θ because equilibrium was reached in a few seconds): $d \sim t^{\mu}$, where $\mu = 1 \pm 0.25$ in the continuous growth stage and $\mu = 0.75 \pm 0.06$ in the coalescence stage. The first exponent value indicates an incomplete condensation (*23*) of Pd on the substrate [as expected at 650 K, where the sticking coefficient for Pd on MgO(001) is small (*2*)] and growth through a direct adsorption on the particles (*24*). These exponent values are consistent with those determined by Beyssens *et al.* (*25*, *26*) for the growth of breath figures through (i) a condensation scaling with the size of the droplets and (ii) coalescence.

The sensitivity of in situ GISAXS to the ordering of the particles and to buried interfaces is illustrated by an archetype of self-organized growth, Co on Au(111) (*11*). When deposited on the $22 \times \sqrt{3}$ herringbone reconstruction of the Au(111) surface (*27*, *28*), Co forms a rectangular network of two atomic- layer–high islands (*9*), nucleating and growing on top of the kinks that separate two variants of the reconstruction. The nanodot array has periods of ~7.7 nm along [11$\bar{2}$] and 17 nm along [1$\bar{1}$0]. Figure 4, A and B, shows GISAXS patterns for a 0.02-nm-thick Co deposit, with the incident beam along [1$\bar{1}$0] and [11$\bar{2}$]. Here, $S(\mathbf{q})$ is a set of diffraction rods perpendicular to the surface, with separations inversely proportional to the real-space periodicities. The very narrow diffraction rods shown in Fig. 4A demonstrate the high degree of order along [11$\bar{2}$] (the average domain size is ~300 nm). The much broader rods along (1$\bar{1}$0) (Fig. 4B) reveal short-range order between rows, which was analyzed as a cumulative (or liquidlike) disorder (with a standard deviation of 2.1 nm for a period of 8.5 nm). This disorder is connected to the period fluctuation between the kinks of the herringbone superstructure of the reconstruction, which depends on a subtle energy balance. In addition, a quantitative analysis of the GISAXS patterns allows determination of the exact position of the Co dot located inside the super-unit cell, which evolves from close to the edges of the cell to close to the center as the dot size increases. A marked result is that fixed-position rods of scattering could be measured up to $\Theta = 1.8$ nm of Co deposited (Fig. 4, C and D), well after the film had fully coalesced, which occurred below $\Theta \sim 0.3$ nm. This effect could not be explained by the topography of the Co surface alone and thus implies the existence of a buried microstructure with the same periodicity as the nanodot lattice, even after coalescence and beyond.

High-brightness, very-low-background, and ultra-high-vacuum in situ studies allow 2D GISAXS measurements to be performed during growth of nanoparticles with a very high signal-to-noise ratio. Quantitative analysis yields statistical averages (over the whole sample area) of the shape, size, and size distributions of the growing nanoparticles. The Pd/MgO(001) case illustrates the capability of the method to determine the average morphological parameters of macroscopic collections of particles in a single measurement (typically over a few hours), covering all three stages of nucleation, growth, and coalescence, and to derive growth laws. The Co/Au(111) example shows that in situ GISAXS could be very helpful to determine the best conditions for self-organized growth, because the data are extremely sensitive to positional order, and to probe buried interfaces. The technique enables real-time measurements as a function of either deposition time or annealing temperature, because conditions in which the acquisition time is short with respect to the kinetics can be easily achieved even for submonolayer amounts.

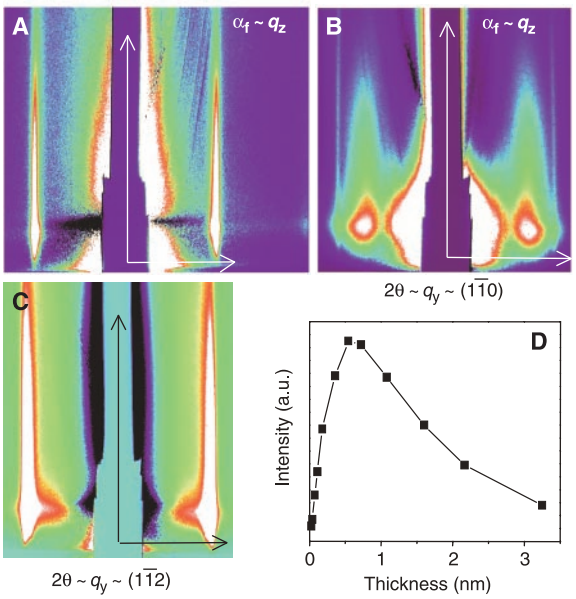

Fig. 4. GISAXS patterns of Co deposits on the herringbone reconstruction of the Au(111) surface for (**A**) $\Theta = 0.02$ nm with the incident beam along Au[1$\bar{1}$0], (**B**) $\Theta = 0.02$ nm and the beam along Au[11$\bar{2}$], and (**C**) $\Theta = 0.6$ nm and the beam along Au[1$\bar{1}$0]. (**D**) Experimental evolution with Θ of the integrated intensity of the first order diffraction rod along (11$\bar{2}$). a.u., arbitrary units.

References and Notes

1. M. Valden, X. Lai, D. W. Goodman, *Science* **281**, 1647 (1998).
2. C. R. Henry, *Surf. Sci. Rep.* **31**, 231 (1998).
3. P. L. Hansen *et al.*, *Science* **295**, 2053 (2002).
4. J. Corno, M. Galtier, D. Renard, *J. Magn. Magn. Mater.* **174**, L10 (1997).
5. Semiconductor Quantum Dots, A. Zunger, Ed. *Mater. Res. Soc. Bull.* **23** (no. 2) (1998).
6. J. R. Levine, J. B. Cohen, Y. W. Chung, P. Georgopoulos, *J. Appl. Cryst.* **22**, 528 (1989).
7. J. Stangl *et al.*, *Appl. Phys. Lett.* **74**, 3785 (1999).
8. M. Schmidbauer *et al.*, *Phys. Rev. B* **58**, 10523 (1998).
9. B. Voigtländer, G. Meyer, N. M. Amer, *Phys. Rev. B* **44**, 10354 (1991).
10. M. Rauscher *et al.*, *J. Appl. Phys.* **86**, 6763 (1999).
11. Materials and methods are available as supporting material on *Science* Online.
12. H. Graoui, S. Giorgio, C. R. Henry, *Surf. Sci.* **417**, 350 (1998).
13. R. Lazzari, *J. Appl. Cryst.* **35**, 406 (2002).
14. We determined the island-size distribution and the pair correlation function by analyzing several transmission electron microscope (TEM) images. In all cases, the lateral size distribution was well fitted by a log-normal function, the usual one encountered in this kind of growth regime. $S(\mathbf{q})$ (Fig. 3B) was computed from the pair correlation function and fitted with an appropriate function that had two parameters to describe the inter-island separation D and the height and width of the first peak.
15. A marked result was the very narrow distribution of particle height with respect to that of lateral size, which is evidenced by the second and third orders of scattering perpendicular to the surface (Figs. 2 and 3A) and confirmed by quantitative analyses. This behavior, which seemed to be independent of the deposited metal [Pd, Ag, or Pt on MgO(001)], temperature, and film thickness, is believed to originate from growth mechanisms. First, the denser (111) faces grow faster than the (001) facets. Second, although the (111) side facets grow from both the vapor phase and atom diffusion, the (001) top facets grow mostly from the vapor phase, as if they were isolated, because of the high-energy barrier an atom has to overcome to jump from a (111) to a (001) facet.
16. For all samples, the thickness measured with the quartz microbalance was recalibrated ex situ on the final deposit by Rutherford backscattering spectroscopy and by x-ray microprobe.
17. The small differences between experimental (Fig. 3A) and simulated (Fig. 3D) images could have arisen from a small amount of already coalesced particles. However, the first islands to coalesce were the smallest, which contributed only negligibly to the GISAXS pattern because the intensity was proportional to the volume squared of the particles.
18. G. Wulff, *Z. Kristallogr.* **34**, 449 (1901).
19. R. Kaishew, thesis, *Arbeitstagung Festköper Physik* Dresden (1952), p. 81.
20. A. Shi, *Phys. Rev. B* **36**, 9068 (1987).

21. A. F. Moodie, C. E. Marble, *Philos. Mag.* **35**, 201 (1977).
22. G. Haas *et al.*, *Phys. Rev. B* **61**, 11105 (2000).
23. D. Kashchiev, *Thin Solid Films* **55**, 399 (1978).
24. C. L. Liu, J. M. Cohen, J. B. Adams, A. F. Voter, *Surf. Sci.* **253**, 334 (1991).
25. J.-L. Viovy, D. Beyssens, C. M. Knobler, *Phys. Rev. A* **37**, 4965 (1988).
26. D. Beyssens, C. M. Knobler, *Phys. Rev. Lett.* **57**, 1433 (1986).
27. J. Barth, H. Brune, G. Ertl, R. Behm, *Phys. Rev. B* **42**, 9307 (1990).
28. A. R. Sandy, S. G. J. Mochrie, D. M. Zehner, K. G. Huang, D. Gibbs, *Phys. Rev. B* **43**, 4667 (1991).
29. We thank all the staff of the ESRF ID32 beamline for their invaluable help during the mounting of the GISAXS setup and the measurements.

Supporting Online Material
www.sciencemag.org/cgi/content/full/300/5624/1416/DC1
Materials and Methods
Figs. S1 to S3
References and Notes
Movie S1

7 January 2003; accepted 14 April 2003

Atomic Resolution Imaging of a Carbon Nanotube from Diffraction Intensities

J. M. Zuo,[1]* I. Vartanyants,[2]† M. Gao,[1] R. Zhang,[3] L. A. Nagahara[3]

Atomic imaging of three-dimensional structures has required a crystal in diffraction or a lens in electron imaging. Whereas diffraction achieves very high resolution by averaging over many cells, imaging gives localized structural information, such as the position of a single dopant atom. However, lens aberrations limit electron imaging resolution to about 1 angstrom. Resolution is reduced further by low contrast from weak scattering or from the limitations on electron dose for radiation-sensitive molecules. We show that both high resolution and high contrast can be achieved by imaging from diffraction with a nanometer-sized coherent electron beam. The phase problem is solved by oversampling and iterative phase retrieval. We apply this technique to image a double-wall carbon nanotube at 1-angstrom resolution, revealing the structure of two tubes of different helicities. Because the only requirement for imaging is a diffraction pattern sampled below the Nyquist frequency, our technique has the potential to image nonperiodic nanostructures, including biological macromolecules, at diffraction intensity–limited resolutions.

Structure determination for crystals is currently performed with the use of x-ray and neutron diffraction, which average over many identical cells by focusing beams into directions defined by the crystal's reciprocal lattice. Local internal structures are imaged with the use of transmission electron microscopes. Resolution at ~1 Å for crystalline samples is possible with recent developments in microscopy (*1*–*3*). However, many nanostructures have not been accessible to crystallography. For example, nonperiodic nanostructures lack well-defined atomic columns and cannot be imaged in projection at current microscope resolutions. The resolution for samples that are radiation-sensitive can be further reduced by low imaging contrast from the low electron dose. In cases of biological macromolecules, atomic resolution requires an averaging of over $\geq 10^5$ molecules of the same configuration in cryoelectron microscopy (*4*).

To realize atomic resolution unlimited by microscope lens aberrations and contrast transfer functions, we used nanoarea electron diffraction (NAED) for imaging. We recorded the intensities of electron diffraction waves (or diffraction patterns) from a single double-wall carbon nanotube (DWNT) (*5*) with the use of a nanometer-sized coherent electron beam. The diffraction intensities were measured in reciprocal space at a resolution finer than the frequency of one over the sample size (the Nyquist frequency). This approach is alternatively called oversampling (*6*). Recorded intensities give only the amplitude of the diffracted wave. Direct imaging of the object requires both the amplitude and the phase of the wave function. The missing phase information is known as the phase problem. However, recent studies have shown that, in dimensions more than one, the phase problem is uniquely solvable for localized objects (*7*–*9*). The missing phase can be retrieved ab initio from diffraction intensities through an iterative procedure (*10*–*12*). We applied this approach to experimental electron diffraction patterns. The results show that this technique is capable of finding unique solutions independent of the starting phases. The approach of diffractive imaging, or imaging from diffraction intensities, appears to solve many technical difficulties in conventional imaging, namely, resolution limitations from lens aberration, sample drift, instrument instability, and low contrast in electron images.

We imaged a DWNT because of the challenge of seeing carbon and the importance of structure to its properties. The structure of a perfect carbon nanotube is a rolled-up graphene strip whose geometry is completely specified by the circumferential period, or the chiral vector, $\mathbf{c} = n\mathbf{a} + m\mathbf{b}$ ($\mathbf{a}$ and $\mathbf{b}$ are unit cell vectors of graphite, $\mathbf{a}\hat{}\mathbf{b} = 60°$, and n and m are integers) (*13*). Electron scattering by carbon is weak, and contrast in transmission electron microscopy (TEM) images has thus far been too low to see the atomic structure. Because both helical structure and carbon are common among biological single particles, DWNTs are excellent samples for testing imaging resolution and sensitivity. Also, the mechanical and electric properties of a nanotube depend on its structure (*14*). However, to date, only the outermost shell of a carbon nanotube has been imaged by scanning tunneling microscopy with atomic resolution (*15*).

To record an electron diffraction pattern from a single DWNT, we used coherent electron nanodiffraction in a JEOL (Peabody, MA) electron microscope with a field emission gun. Low-resolution electron imaging was used to locate and select the tube. Figure 1 shows the recorded electron diffraction pattern and a schematic ray diagram. The demagnified condenser aperture, rather than a focused spot (*16*), is used to limit the beam size at the sample. For an aperture 10 μm in diameter, the electron beam diameter is ~50 nm. The small probe size allows us to select a section of the tube for electron diffraction. The field emission gun provides both coherence and a high beam intensity with the probe current intensity at $\sim 10^5$ electron (e) $s^{-1}\cdot nm^2$. The electron diffraction patterns were recorded on electron imaging plates (*17*).

Information about structure is contained in the diffraction pattern recorded at far field from the sample. For carbon nanotubes, electron scattering is weak and well described by the kinematic approximation

$$I(\mathbf{k}) \propto \left| \int_{-\infty}^{\infty} \phi(\mathbf{r})[1 + i\pi\lambda U(\mathbf{r})]\exp(2\pi i\mathbf{k}\cdot\mathbf{r})d\mathbf{r} \right|^2 \quad (1)$$

Here, $U(\mathbf{r})$ equals $2m|e|V(\mathbf{r})/h^2$, with $V(\mathbf{r})$ as the Coulomb potential of the sample. The

[1]Department of Materials Science and Engineering, [2]Department of Physics, F. Seitz Materials Research Laboratory, University of Illinois at Urbana-Champaign, IL 61801, USA. [3]Physical Sciences Research Laboratories, Motorola Labs, 7700 South River Parkway, Tempe, AZ 85284, USA.

*To whom correspondence should be addressed. E-mail: jianzuo@uiuc.edu
†On leave from Institute of Crystallography Russian Academy of Science, Leninsky Prospekt. 59, 117333 Moscow, Russia.